Journal of Mathematical Imaging and Vision, to appear

Parameter-Free Elastic Deformation Approach for 2-D and 3-D Registration Using Prescribed Displacements

Wladimir Peckar, Christoph Schnörr, Karl Rohr, and H. Siegfried Stiehl

Universität Hamburg, FB Informatik, AB Kognitive Systeme,
Vogt-Kölln-Str. 30, D-22527 Hamburg, Germany

November 11, 1998

Abstract

A *parameter-free* approach for non-rigid image registration based on elasticity theory is presented. In contrast to traditional physically-based numerical registration methods, no forces have to be computed from image data to drive the elastic deformation. Instead, displacements obtained with the help of mapping boundary structures in the source and target image are incorporated as hard constraints into elastic image deformation. As a consequence, our approach does not contain any parameters of the deformation model such as elastic constants. The approach guarantees the *exact* correspondence of boundary structures in the images assuming that correct input data are available. The implemented incremental method allows to cope with *large* deformations. The theoretical background, the finite element discretization of the elastic model, and experimental results for 2-D and 3-D synthetic as well as real medical images are presented.

Keywords: Non-rigid medical image registration, elasticity theory, finite element method

1 Introduction

One of the most important problems in medical computer vision is image registration. The combination of data from different individuals, different modalities, as well as image-atlas registration, helps to locate structures in the images and, therefore, gives improved information in clinical applications. A typical example is the registration of brain tomograms. For registration, a three-dimensional (3-D) *source* image has to be completely transformed onto the *target* image. Important criteria are accuracy and robustness of the registration procedure. Due to significant individual anatomical variabilities and large amounts of data to be processed (in particular, in case of 3-D images), the development of efficient computational methods for registration purposes is a rather difficult task.

Because of anatomical variability, *rigid* registration methods [32], [22], [16] do not usually yield good results for general registration problems and, therefore, methods that allow *non-rigid* transformations must be applied. There are several different non-rigid registration techniques known from the literature.

Landmark-based methods [4], [34], [21] require a set of interactively or automatically defined so-called landmarks or points for which the correspondences are supposed to be known while the deformation of the rest of the image is computed by using spline interpolation or approximation.

In *surface-based* methods [39], [40], the complete volumetric deformation of the source image is interpolated to agree with pre-computed surface warps.

Another group of methods dealing with non-rigid image registration is the *physically-based numerical* methods where non-rigid transformations are modeled as deformations of physical bodies (solids, fluids) [2], [10], see also Section 2. The traditional image registration scheme using physically-based numerical methods is the following: Forces are first derived from image data using some similarity measure and then applied to deform the source image driving it to a correspondence with the target image. The required deformation is then obtained from the numerical solution of the corresponding motion equation of the underlying material.

In the present paper, we propose a parameter-free registration approach based on elasticity theory which guarantees the exact correspondence of certain structures from the source and target image under the assumption that correct input data are available. Instead of forces, we use as input data in our model point correspondences (displacements) obtained by mapping boundary structures such as the outer cortical boundary and the boundary of the ventricles from the source image to those from the target image. The source image is then elastically deformed with displacements incorporated as hard constraints in addition to the conditions on the image boundary, while the rest of the source image is deformed together with the boundary structures.

The proposed approach has several advantages compared to traditional methods. i) No forces have to be derived from image data to drive the elastic deformation. For multi-modal images using a local similarity measure, this is known to be a difficult problem. ii) As a consequence, the remaining parameters of the deformation model (elastic constants) drop out from the model and it becomes completely *parameter-free*. iii) It can always be guaranteed that the required deformation is obtained and that certain structures in the source image are *exactly* matched with those of the target image due to the constraints. iv) Registration methods based on elasticity theory traditionally assume that only small deformations take place. Since this is not always the case in real applications, we use the *Lagrangian incremental method* to compute *large* deformations.

We implemented a discretization of the elastic model on the basis of the *finite element method* (FEM). By varying the size of the finite elements, one can easily define how close the discrete solution will be to the continuous one. The discrete representation of our model is also well-suited for treatment of complicated boundary conditions (irregularly shaped, possibly interactively specified, domains), where the usability of traditionally implemented finite differences is limited.

2 Relationship to other work

In this section, we briefly review the literature related to the application of physically-based numerical models to the registration of brain images.

Broit [7] was the first who used a model derived from elasticity theory to match two- and three-dimensional brain images. He defined a cross-correlation coefficient between local regions in two images to derive forces that drive the elastic "rubber-sheet" deformation of the source image onto the target one. The implemented linear model assumed small deformations. It has been improved [2], [36] to increase the speed of computations and to avoid local minima. A probabilistic model based on the finite element method, which has been reported to have properties similar to those of [7], [2], has been proposed in [24].

Because of the potentially large variability of anatomical structures in the human brain, possible deformations by the registration of brain images are not limited to locally small displacements. To cope with this problem, another group of physically-based numerical methods based on the theory of fluid mechanics has been introduced by Christensen et al. [10], [11]. (In addition to fluid methods, one can also mention the hyperelastic approach of Rabbitt et al. [33] where the same sensor model for forces derivation is used.) These models exploit the property that fluids do not carry memory about their initial state. The mathematical model involves a representation of the source image as a viscous compressible fluid and can be applied for the computation of large non-linear deformations. Formally, the derived fluid model looks analogous to the linear elastic one. The fundamental difference is, however, that it is dynamic and an extra equation is used to update the values of the displacement field in each iteration step. The original fluid model has been improved to increase the speed of the approach [5], [6]. A common drawback with the approaches mentioned above is that a local intensity-based similarity measure is still used for derivation of forces. This considerably limits the applicability of the introduced fluid model as a general tool for registration problems, since local minima of the similarity function do not guarantee an exact global match. In particular, this is the case for non-rigid multi-modality matching where the image function alone is not a reliable feature for measuring similarity between images.

Davatzikos et al. [20], [18] proposed a linear elastic model based on a boundary mapping where no local similarity measure is used. The elastic deformation is driven by external forces obtained from mapping parametric representations of the outer cortical surface and the boundary of the ventricles. The deformable surface algorithm is applied to the source and target image to obtain a one-to-one mapping of boundary structures. The source image is represented as elastic inhomogeneous material. This allows parts of the image, for example the ventricles, to deform more freely. A drawback of this approach is the dependence on the parameters of the deformation model (elastic constants) which need to be determined empirically to obtain best results. Note, that with this approach it is principally possible to obtain exact correspondences of boundary structures by using sufficiently small values of the parameters. However, this makes the model potentially numerically unstable, especially for parallel realization, where the usage of efficient preconditioners is limited. Another drawback is that the currently implemented linear model assumes only small deformations.

The approach developed in the present paper is closely related to the one in [20], [18]. The principal difference is, however, that no external forces have to be explicitly used. As a consequence, no parameters of the deformation model are required for our approach. We incorporate known displacements as hard constraints in the model. This allows the *exact* matching of those structures for which the displacements were defined. The approach is numerically stable. In contrast to the linear elastic model implemented in [20], [18] which assumes only small deformations, we use the incremental method to compute *large* deformations.

In the remainder of this paper, we present our registration approach, its numerical implementation, and experimental results. Particularly, this includes the derivation of the linear elastic and incremental model, the outlines of the existence theory, the finite element discretization, the incorporation of constraints, and the elimination of parameters from the models.

3 Approach

In this section, we formally describe our registration approach. We start with some definitions from the theory of three-dimensional mathematical elasticity and present a general non-linear elastic registration model. Then we describe the derivation of the linear elastic and incremental elastic model, their variational formulations, and their finite element discretization. We conclude with the numerical implementation of the models considering the application to non-rigid image registration.

3.1 Elastic registration model

In the following, we describe a general non-linear registration model based on elasticity theory. Our presentation of basic notions from three-dimensional elasticity and notation follow mainly

[13].

Elastic image registration can be formulated as a state of equilibrium on the source image represented as an elastic solid which is deformed by applying external forces. External forces are usually derived to minimize some cost function measuring similarity between the source and target image [7], [2], [10]. Assuming external forces are given, we have to compute a corresponding deformation of the source image which brings both images into correspondence.

We call the *image domain* an open, bounded, connected subset Ω of $\mathbb{R}^3$ with a Lipschitz-continuous boundary Γ. We define a *deformation* of the image as a smooth orientation-preserving vector field $\boldsymbol{\phi} : \bar{\Omega} \longrightarrow \mathbb{R}^3$ such that for $\mathbf{x} \in \bar{\Omega}$

$$\boldsymbol{\phi}(\mathbf{x}) = \mathbf{x} + \mathbf{u}(\mathbf{x}), \tag{1}$$

where the vector field $\mathbf{u} : \bar{\Omega} \longrightarrow \mathbb{R}^3$ is called the *displacement field*.

To perform the elastic registration, we have to find a solution of the non-linear equation

$$\mathbf{A}(\mathbf{u}) = \mathbf{f} \tag{2}$$

with corresponding boundary conditions where $\mathbf{f} : \Omega \longrightarrow \mathbb{R}^3$ denotes here a known vector of applied forces, and $\mathbf{A}$ is the non-linear *elasticity operator* defined later in this section.

Equilibrium equations

We first give some definitions from elasticity theory.

As a measure of local deformation, the *deformation gradient* $\boldsymbol{\nabla\phi}$ is defined as a matrix $(\boldsymbol{\nabla\phi})_{ij} = \partial_j \phi_i$, $\det(\boldsymbol{\nabla\phi}) > 0$. With the help of the deformation gradient, the symmetric *Cauchy-Green strain tensor* is introduced as $\mathbf{C} = \boldsymbol{\nabla\phi}^{\mathrm{T}}\boldsymbol{\nabla\phi}$. If $\mathbf{C} = \mathbf{I}$, the deformation is called *rigid*.

Since we have $\boldsymbol{\nabla\phi} = \mathbf{I} + \boldsymbol{\nabla}\mathbf{u}$,

$$\mathbf{C} = \boldsymbol{\nabla\phi}^{\mathrm{T}}\boldsymbol{\nabla\phi} = \mathbf{I} + \boldsymbol{\nabla}\mathbf{u}^{\mathrm{T}} + \boldsymbol{\nabla}\mathbf{u} + \boldsymbol{\nabla}\mathbf{u}^{\mathrm{T}}\boldsymbol{\nabla}\mathbf{u}. \tag{3}$$

The *Green-St. Venant strain tensor* $\mathbf{E}$ measures how close the deformation is to the rigid one:

$$\mathbf{E}(\mathbf{u}) = \frac{1}{2}(\mathbf{C} - \mathbf{I}) = \frac{1}{2}(\boldsymbol{\nabla}\mathbf{u}^{\mathrm{T}} + \boldsymbol{\nabla}\mathbf{u} + \boldsymbol{\nabla}\mathbf{u}^{\mathrm{T}}\boldsymbol{\nabla}\mathbf{u}). \tag{4}$$

The *equilibrium equations* over the image $\bar{\Omega}$, with applied body forces $\mathbf{f} : \Omega \longrightarrow \mathbb{R}^3$ acting on its interior Ω and applied surface forces $\mathbf{g} : \Gamma_1 \longrightarrow \mathbb{R}^3$ acting on a portion of its boundary $\Gamma_1 \subset \Gamma$, can be formulated as [13]:

$$\begin{cases} -\mathbf{div}\,\mathbf{T}(\mathbf{x}) = \mathbf{f}(\mathbf{x}) & \text{in } \Omega, \\ \mathbf{T}(\mathbf{x})\mathbf{n} = \mathbf{g}(\mathbf{x}) & \text{on } \Gamma_1, \end{cases} \tag{5}$$

where $\mathbf{T}(\mathbf{x}) : \bar{\Omega} \longrightarrow \mathbb{R}^{3\times 3}$ denotes the unknown *first Piola-Kirchhoff stress tensor*, and $\mathbf{n}$ is the outer unit vector normal to Γ_1. By using the symmetric *second Piola-Kirchhoff stress tensor* $\boldsymbol{\Sigma}(\mathbf{x}) = \boldsymbol{\nabla\phi}(\mathbf{x})^{-\mathbf{1}}\mathbf{T}(\mathbf{x})$, the equilibrium equations take the form:

$$\begin{cases} -\mathbf{div}\,\{\boldsymbol{\nabla\phi}(\mathbf{x})\,\boldsymbol{\Sigma}(\mathbf{x})\} = \mathbf{f}(\mathbf{x}) & \text{in } \Omega, \\ \boldsymbol{\nabla\phi}(\mathbf{x})\,\boldsymbol{\Sigma}(\mathbf{x})\mathbf{n} = \mathbf{g}(\mathbf{x}) & \text{on } \Gamma_1. \end{cases} \tag{6}$$

We assume that images are represented as St. Venant-Kirchhoff elastic material for which the second Piola-Kirchhoff stress tensor depends only on the Green-St. Venant strain tensor and can be written as

$$\boldsymbol{\Sigma}(\mathbf{x}) = \bar{\boldsymbol{\Sigma}}(\mathbf{E}) = \lambda\,\mathrm{tr}(\mathbf{E})\mathbf{I} + 2\mu\mathbf{E}. \tag{7}$$

The two positive constants λ and μ are called the *Lamé elastic constants*.

With the help of the last equation, the equilibrium equations become:

$$\left\{ \begin{array}{l} -\mathbf{div}\,\{(\mathbf{I}+\boldsymbol{\nabla}\mathbf{u})\,\bar{\boldsymbol{\Sigma}}(\mathbf{E}(\mathbf{u}))\} = \mathbf{f} \;\text{ in } \Omega, \\ (\mathbf{I}+\boldsymbol{\nabla}\mathbf{u})\,\bar{\boldsymbol{\Sigma}}(\mathbf{E}(\mathbf{u}))\mathbf{n} = \mathbf{g} \;\text{ on } \Gamma_1. \end{array} \right. \tag{8}$$

Boundary conditions

A very important point is the choice of appropriate boundary conditions. In brain images, regions of interest are often situated far away from the boundaries of the image. For such purposes, the homogeneous Dirichlet boundary condition ($\mathbf{u} = \mathbf{0}$ on Γ, $\Gamma_1 = \emptyset$) seems to be applicable. By using this boundary condition, we force the preservation of image dimensions and allow the regions of interest to deform freely.

By applying the homogeneous Dirichlet boundary condition to the equilibrium equations and assuming that the driving forces are given, we receive the displacement field for registration as a solution of the system:

$$\left\{ \begin{array}{l} \mathbf{A}(\mathbf{u}) = \mathbf{f} \;\text{ in } \Omega, \\ \mathbf{u} = \mathbf{0} \;\text{ on } \Gamma, \end{array} \right. \tag{9}$$

where $\mathbf{A}(\mathbf{u}) = -\mathbf{div}\,\{(\mathbf{I}+\boldsymbol{\nabla}\mathbf{u})\,\bar{\boldsymbol{\Sigma}}(\mathbf{E}(\mathbf{u}))\}$ is the non-linear elasticity operator. Since $\Gamma_1 = \emptyset$, the boundary condition on it is dropped.

3.2 Derivation of the linear elastic model

In this section, we derive the linear elastic model which we used in our registration scheme. Our approach is based on the *variational formulation* of the linearized equilibrium equations. The importance and advantage of the variational formulation is that we can use it for the proof of the existence and uniqueness of the solution and, moreover, that it is directly related to the finite element discretization of the linearized equilibrium equations, since the discrete problem inherits properties of the continuous model.

We first set λ to zero to eliminate one degree of freedom from the model. As a result, objects in images are allowed to grow without being laterally shrunk. This is impossible for real materials for which $\lambda > 0$ and $\mu > 0$, but it is a quite useful property for non-rigid registration problems taking into account significant size variability of objects in brain images (see, for example, [2]). The remaining parameter μ will be eliminated by incorporating prescribed displacements (see Section 3.5) to make the registration model completely parameter-free.

To obtain a linearization of (9), we compute the derivative at $\mathbf{u} = \mathbf{0}$ of the operator of non-linear elasticity $\mathbf{A}$. The term $\mathbf{A}'(\mathbf{0})\mathbf{u}$ is given as [13]: $\mathbf{A}'(\mathbf{0})\mathbf{u} = -\mathbf{div}\,\{\lambda\,\mathrm{tr}(\mathbf{e}(\mathbf{u}))\mathbf{I} + 2\mu\mathbf{e}(\mathbf{u})\}$, so the linearization of (9) with the parameter λ excluded can be written as:

$$\left\{ \begin{array}{l} -\mathbf{div}\,\mathbf{e}(\mathbf{u}) = \dfrac{1}{2\mu}\mathbf{f} \;\text{ in } \Omega, \\ \mathbf{u} = \mathbf{0} \;\text{ on } \Gamma, \end{array} \right. \tag{10}$$

where $\mathbf{e}(\mathbf{u}) = \frac{1}{2}\left(\boldsymbol{\nabla}\mathbf{u}^{\mathrm{T}} + \boldsymbol{\nabla}\mathbf{u}\right)$ is the *linearized strain tensor*. We transferred the parameter μ to the right-hand side of (10) to stress that the solution of the simplified problem is now completely determined by the applied forces.

To obtain a variational formulation of (10), we first define a normed vector space

$$\mathbf{V} := \{\mathbf{v} \in (H^1(\Omega))^3;\ \mathbf{v} = \mathbf{0} \;\text{ on }\; \Gamma\}. \tag{11}$$

By taking scalar product with *test functions* $\mathbf{v} \in \mathbf{V}$, we obtain a variational formulation of (10) as

$$-\int_\Omega \mathbf{div}\,\mathbf{e}(\mathbf{u}) \cdot \mathbf{v}\, dx = \frac{1}{2\mu} \int_\Omega \mathbf{f} \cdot \mathbf{v}\, dx, \tag{12}$$

or componentwise

$$\int_\Omega \sum_{j,p,q=1}^{3} a_{ijpq} e_{pq}(\mathbf{u}) \partial_j v_i\, dx = \frac{1}{2\mu} \int_\Omega f_i v_i\, dx, \tag{13}$$

where $a_{ijpq} = \frac{1}{2}(\delta_{ip}\delta_{jq} + \delta_{iq}\delta_{jp}),\ i,j,p,q = 1,2,3,\ \delta_{ij}$ is Kronecker's symbol, and dx is the volume element in the source image domain Ω.

By using Green's formula and the fact that the test functions vanish on the boundary Γ, the variational formulation of (10) written in form of abstract variational problem [12] becomes: Find $\mathbf{u} \in \mathbf{V}$ such that

$$a(\mathbf{u}, \mathbf{v}) = l(\mathbf{v}), \quad \forall \mathbf{v} \in \mathbf{V}, \tag{14}$$

where the symmetric bilinear form $a(\mathbf{u}, \mathbf{v})$ and the linear form $l(\mathbf{v})$ are defined as:

$$a(\mathbf{u}, \mathbf{v}) = \int_\Omega \langle \mathbf{e}(\mathbf{u}), \mathbf{e}(\mathbf{v}) \rangle\, dx, \tag{15}$$

$$l(\mathbf{v}) = \frac{1}{2\mu} \int_\Omega \mathbf{f} \cdot \mathbf{v}\, dx. \tag{16}$$

The existence result for the abstract variational problem (14) is given in Appendix B.

3.3 FEM discretization of the linear elastic model

In this section, we present the FEM discretization of the variational problem (14) in the 3-D case. For discretization, we use the *Galerkin method* [12], [17].

We seek the discrete solution to the problem: Find $\mathbf{u}_N \in \mathbf{V}_N \subset \mathbf{V},\ \mathbf{V}_N := \mathrm{span}\{\boldsymbol{\phi}_1, \boldsymbol{\phi}_2, \ldots, \boldsymbol{\phi}_N\}$ such that

$$a(\mathbf{u}_N, \mathbf{v}_N) = l(\mathbf{v}_N), \quad \forall \mathbf{v}_N \in \mathbf{V}_N, \tag{17}$$

where:

$$a(\mathbf{u}_N, \mathbf{v}_N) = \int_\Omega \langle(\mathbf{e}(\mathbf{u}_N), \mathbf{e}(\mathbf{v}_N)\rangle\, dx, \tag{18}$$

$$l(\mathbf{v}_N) = \frac{1}{2\mu} \int_\Omega \mathbf{f} \cdot \mathbf{v}_N\, dx. \tag{19}$$

By representing the functions $\mathbf{u}_N$ and $\mathbf{v}_N$ as weighted sums of basis functions spanning the subspace $\mathbf{V}_N$, we receive:

$$\mathbf{u}_N = \sum_{i=1}^{N} u_i \boldsymbol{\phi}_i, \qquad \mathbf{v}_N = \sum_{j=1}^{N} v_j \boldsymbol{\phi}_j, \tag{20}$$

and

$$\sum_{i,j=1}^{N} u_i v_j a(\boldsymbol{\phi}_i, \boldsymbol{\phi}_j) = \sum_{j=1}^{N} v_j l(\boldsymbol{\phi}_j). \tag{21}$$

Since three components of the unknown vector field need to be determined, the number of nodal points for discretization is $N/3$. One usually chooses nodal points to correspond to image voxels, so the number of nodal points is equal in this case to the product of image dimensions.

The solution vector $\mathbf{u} = \{u_i\}$ is obtained as a solution of the system of linear equations:

$$\sum_{i=1}^{N} u_i \int_\Omega \sum_{k,l=1}^{3} e_{kl}(\boldsymbol{\phi}_i) e_{kl}(\boldsymbol{\phi}_j)\, dx = \frac{1}{2\mu} \int_\Omega \mathbf{f} \cdot \boldsymbol{\phi}_j \, dx; \quad j = 1, \ldots, N. \tag{22}$$

The system (22) can be written in matrix form as

$$\underbrace{\begin{pmatrix} \mathbf{A}_{11} & \mathbf{A}_{12} & \mathbf{A}_{13} \\ \mathbf{A}_{21} & \mathbf{A}_{22} & \mathbf{A}_{23} \\ \mathbf{A}_{31} & \mathbf{A}_{32} & \mathbf{A}_{33} \end{pmatrix}}_{\mathbf{A}} \underbrace{\begin{pmatrix} \mathbf{u}_1 \\ \mathbf{u}_2 \\ \mathbf{u}_3 \end{pmatrix}}_{\mathbf{u}} = \underbrace{\begin{pmatrix} \mathbf{b}_1 \\ \mathbf{b}_2 \\ \mathbf{b}_3 \end{pmatrix}}_{\mathbf{b}}, \tag{23}$$

where:

$$A_{11,\,ij} = a\left(\begin{pmatrix} \phi_i \\ 0 \\ 0 \end{pmatrix}, \begin{pmatrix} \phi_j \\ 0 \\ 0 \end{pmatrix} \right) = \int_\Omega \{2\, \partial_1\phi_i \partial_1\phi_j + \partial_2\phi_i\partial_2\phi_j + \partial_3\phi_i\partial_3\phi_j\}\, dx; \quad i, j = 1, \ldots, N/3, \tag{24}$$

$$A_{12,\,ij} = a\left(\begin{pmatrix} \phi_i \\ 0 \\ 0 \end{pmatrix}, \begin{pmatrix} 0 \\ \phi_j \\ 0 \end{pmatrix} \right) = \int_\Omega \partial_2\phi_i\partial_1\phi_j \, dx; \quad i, j = 1, \ldots, N/3, \tag{25}$$

$$b_{1,\,j} = \frac{1}{\mu} \int_\Omega \mathbf{f}_j \cdot (\phi_j,\ 0,\ 0)^{\mathrm{T}}\, dx = \frac{1}{\mu} \int_\Omega f_{1,\,j}\phi_j \, dx; \quad j = 1, \ldots, N/3, \tag{26}$$

and $\mathbf{f}_j = (f_{1,j}, f_{2,j}, f_{3,j})^{\mathrm{T}}$ is the value of the applied force in the j-th nodal point.

The submatrices $\mathbf{A}_{13}, \ldots, \mathbf{A}_{33}$ and the rest of the vector $\mathbf{b}$ can be computed analogously.

Since the bilinear form $a(\boldsymbol{\phi}_i, \boldsymbol{\phi}_j)$ is symmetric and $\mathbf{V}$-elliptic (see Appendix B), the matrix $\mathbf{A}$ in (23) is symmetric and positive definite.

Partitioning of volumes: Admissible finite elements

From (24)-(26), one can see that only first order derivatives need to be approximated, so the simplest choice of basis functions for the finite element discretization of (14) is linear basis functions. The corresponding finite element is a tetrahedron.

Though one can easily integrate linear basis functions and there are only four nodal points for each finite element, the algorithmic implementation of the partitioning of volumes using tetrahedrons is not simple because it is impossible to use only reference elements (finite elements with the length of all sides equal to 1) and the transformation of basis functions is required to bring them to the reference form.

Hence, if the discrete problem does not have complicated boundary conditions, it is preferable to use finite elements that are easy to implement. The optimal choice in this case appears to be cubic finite element. The corresponding trilinear basis functions are the following:

$$\begin{aligned}
\phi_1 &= (1-x_1)(1-x_2)(1-x_3);\\
\phi_2 &= x_1(1-x_2)(1-x_3);\\
\phi_3 &= x_1x_2(1-x_3);\\
\phi_4 &= (1-x_1)x_2(1-x_3);\\
\phi_5 &= (1-x_1)(1-x_2)x_3;\\
\phi_6 &= x_1(1-x_2)x_3;\\
\phi_7 &= x_1x_2x_3;\\
\phi_8 &= (1-x_1)x_2x_3.
\end{aligned}$$

As an illustration, the reference cubic element and the projection of the function ϕ_1 onto the x_1x_2-plane are shown in Figure 1.

The usage of cubic finite elements increases the number of nodal points in comparison to tetrahedrons, but at the same time reduces the number of elements required for the partitioning. For practical applications, an adaptive discretization can be implemented, where the fine discretization only needs to be applied to a part of the source image (for example, the common bounding box). This can substantially reduce the problem dimension.

3.4 Definition of prescribed displacements

As input data, our approach requires displacements defined on a subset of the source image. By using the regularizational properties of the elastic deformation, we only need to define displacements on some boundary structures in the image, while the rest of the source image is forced to deform together with these boundary structures. The criteria for choosing certain boundary structures are that they are present and relatively easy to find in both the source and target image. Examples for such structures in brain images are the cortical boundary and the surface of the ventricle system. In this section, we briefly discuss principal methods suitable for the definition of prescribed displacements.

The first possibility is to use some *deformable model* to find boundary structures. The main advantage of the usage of deformable models is that no explicit extraction of object boundaries is needed, and the desired boundary mapping is readily obtained as a mapping of discrete representations of deformable surfaces. The mostly known deformable models are active contours of Kass et al., also known as *snakes* [27], and *balloons*, the extension of snakes to three dimensions [15]. The main drawback of the snake model is that it may converge towards some local minima in the image. The snake model has been improved to make it more robust [14], but its application to real medical images is still limited because of their high complexity. In Section 4, we provide an example where snakes are used to determine the input data for 2-D registration. Other examples of the application of the snake model for obtaining point correspondences have been given in [31]. In [35], the snake model has been extended to a 3-D deformable spline model which has been used to obtain parametric representation of the cortical surface. In [19], another deformable surface algorithm has been introduced for the

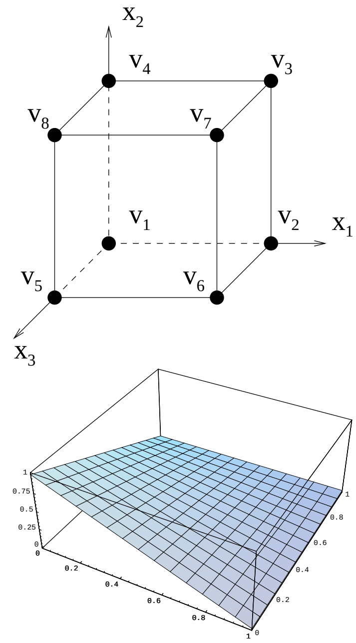

Figure 1: Cubic reference element and the projection of the function ϕ_1 onto the x_1x_2-plane

same purpose. Promising seems also the usage of *geometric deformable models* [9] which are reported to be stable and robust approach for 2-D and 3-D segmentation.

Alternatively to using deformable models, one can also extract object boundaries in both the source and target image and then use some matching techniques, e.g. the *minimal distance algorithm* [3] or *curvature-based methods* [1], [26]. The advantage of such explicit segmentation is that we directly work with boundaries of the objects and not with their approximations obtained by using deformable models. The main drawback is, of course, that segmentation of real brain images is an expensive operation which often requires human interaction. Another drawback is that there are still significant problems in matching of brain structures because of the high complexity of medical data.

To illustrate the principal performance of our registration approach, we implemented for the experiments in Section 4 in addition to the snake model a very simple matching technique based on the 3-D minimal distance algorithm. The development of more advanced methods to obtain point correspondences, as mentioned in the above discussion, is a serious separate problem and is out of the scope of this paper.

For segmentation, we apply a simple thresholding operation. With this procedure, the principal structures such as the skull, the brain, and the ventricle system can be separated by setting appropriate values for intensity thresholds. Then, the connected components of the image after applying the thresholding operation are labeled and, as a result, the desired objects can manually be extracted from the data set by selecting appropriate values of the labels.

The boundaries of the segmented structures are computed by using an edge detector based on the symmetric exponential filter [38] and are represented as sets of points. We defined a prescribed displacement $\mathbf{u}(\mathbf{x})$ as:

$$\mathbf{u}(\mathbf{x}) = \tilde{\mathbf{x}} - \mathbf{x} \quad \text{and} \quad |\mathbf{u}(\mathbf{x})| = \min_{\tilde{\mathbf{x}} \in T} d(\mathbf{x}, \tilde{\mathbf{x}}), \tag{27}$$

where $\mathbf{x} \in S$ and $\tilde{\mathbf{x}} \in T$ denote points in the source and target image, S and T are the corresponding sets of boundaries, and d is the 3-D Euclidean distance. The drawback of the mapping obtained by using the minimal distance algorithm is that it is generally not injective. But from experimental results, we can conclude that for smooth surfaces this takes almost no effect on registration results because of the regularizational properties of the elastic transformation.

In order to improve the registration performance, it is desirable to bring the source and target image possibly close to each other prior to the elastic transformation. Hence, a global transformation needs first to be performed to compensate translational, rotational and scaling differences between the images. Since the gross shape of brains of different individuals is similar, we applied for this purpose in our experiments the principal axes transformation as proposed in [2].

3.5 Incorporation of prescribed displacements and parameter elimination

The two most important features of our approach are i) that it is possible to incorporate prescribed displacements into the discrete model and ii) that the approach is completely parameter-free. In Appendix B, it is shown that the solution of (14) exists and is unique. Thus, we can always restore a unique vector field of applied forces that causes the required deformation. Consequently, such force field also exists and is unique when fixing a subset of the solution of (14). The incorporation of prescribed displacements requires a modification of the original system (22) as described below.

The incorporation of prescribed values which are different from zero into a linear system of equations requires i) a modification of the vector on the right-hand side to consider contributions of the prescribed elements to the system, and ii) a matrix modification [37]. We suppose that a known subset $\tilde{\mathbf{u}}$ of the solution is prescribed on a fixed subset of the image, for example boundaries of some objects with the absence of explicit external forces, so the vector $\mathbf{f}$ in the original system (22) is set to zero. As a result, the remaining parameter μ disappears together with the right-hand side from the original system, which makes our model completely parameter-free.

We obtain now our solution from the modified system:

$$\tilde{\mathbf{A}}\mathbf{u} = \tilde{\mathbf{b}}, \tag{28}$$

where $\tilde{\mathbf{A}}$ is the transformed matrix, and the vector $\tilde{\mathbf{b}}$ contains contributions from the known subset $\tilde{\mathbf{u}}$ of the solution.

For example, to incorporate the prescribed value u_i of the displacement field to the original system, we subtract the product $u_i\mathbf{A^i}$ from its right-hand side ($\mathbf{A^i}$ denotes here the i-th column of $\mathbf{A}$) and put u_i to the i-th position in $\tilde{\mathbf{b}} = \mathbf{b} - u_i\mathbf{A^i} = -u_i\mathbf{A^i}$, since $\mathbf{b} = \mathbf{0}$. Then, analogously to the incorporation of the homogeneous boundary condition, we transform the matrix $\mathbf{A}$ in (23) by filling its i-th row and column with 0 and setting the element a_{ii} to 1. If we prescribe all values of the solution, we will obviously have $\tilde{\mathbf{A}} = \mathbf{I}$ and $\tilde{\mathbf{b}} = \tilde{\mathbf{u}}$.

Formally, the above described process can be represented in the following way:

$$\tilde{\mathbf{A}} = \mathbf{A} - \sum_k a_{ik}\mathbf{e}_i\mathbf{e}_k^{\mathrm{T}} - \sum_k a_{ki}\mathbf{e}_k\mathbf{e}_i^{\mathrm{T}} + a_{ii}\mathbf{e}_i\mathbf{e}_i^{\mathrm{T}}, \tag{29}$$

$$\tilde{\mathbf{b}} = ((a_{ii}+1)\mathbf{I} - \mathbf{A})u_i\mathbf{e}_i. \tag{30}$$

In the following two propositions, we determine properties of the transformed matrix $\tilde{\mathbf{A}}$ which are important for the numerical implementation.

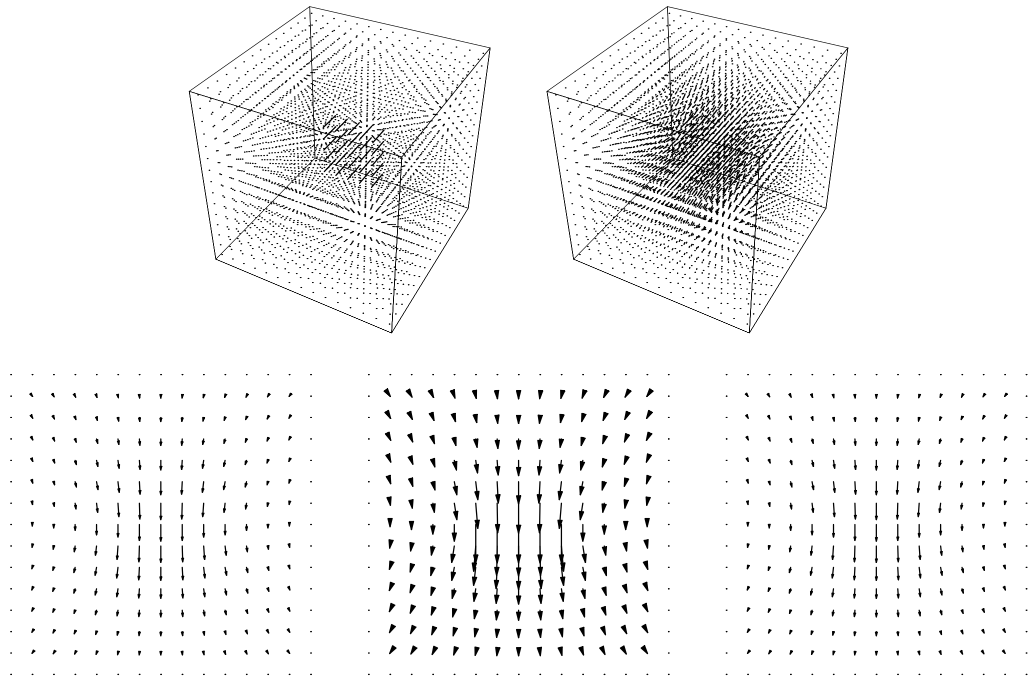

Figure 2: Deformation with prescribed point displacements of a 3-D synthetic image. Top/left: Prescribed displacements. Top/right: Computed 3-D displacement field. Bottom: Horizontal slices 4, 7, 10 from the 3-D computed displacement field above.

Proposition 1 *The transformed matrix* $\tilde{\mathbf{A}}$ *is invertible.*

This is obvious because the original matrix $\mathbf{A}$ is symmetric and positive definite and, therefore, invertible and each row of it contains contributions of more than one finite element, thus the transformed matrix contains no linearly dependent or zero rows and columns and is invertible.

Proposition 2 *The transformed matrix* $\tilde{\mathbf{A}}$ *is symmetric and positive definite.*

The transformed matrix is obviously symmetric, since the incorporation of prescribed displacements equivalently transforms rows and columns of the original symmetric matrix $\mathbf{A}$. A sufficient condition for a matrix to be positive definite is that all its main subdeterminants are positive [23]. Since the determinant of the transformed matrix $\tilde{\mathbf{A}}$ is equal to one of the main subdeterminants of the original positive definite matrix $\mathbf{A}$, the transformed matrix is also positive definite.

Due to the latter results, we always obtain a displacement field from the modified system by incorporating an arbitrary set of prescribed displacements in the model. Limitations are topology violations by defining, for example, large prescribed values due to the linear model or overcrossing displacements.

Figure 2 illustrates the usage of prescribed displacements for a 3-D synthetic image which has the size of 15x15x15 voxels. At the top of the figure, the prescribed displacements (top/left) and the computed displacement field (top/right) are shown. At the bottom of the figure, there are three 2-D horizontal slices from the displacement field above. For this example, slices 4, 7, and 10, starting from the top were chosen. This example illustrates also the usage of the homogeneous Dirichlet boundary condition ($\mathbf{u} = \mathbf{0}$ on Γ, where Γ is the image boundary).

3.6 Numerical implementation

For the solution of the system (28), we used the method of conjugate gradients [25]. To reduce the condition number of the matrix $\tilde{\mathbf{A}}$, we scaled the system with the help of the diagonal matrix $\mathbf{D} = \mathrm{diag}\{d_{11}, \ldots, d_{nn}\}$ (symmetry preserving Jacobi preconditioning):

$$\mathbf{D}^{-1/2}\tilde{\mathbf{A}}\mathbf{D}^{-1/2}\mathbf{D}^{1/2}\mathbf{u} = \mathbf{D}^{-1/2}\tilde{\mathbf{b}}, \tag{31}$$

where $d_{ii}^{-1/2} = \frac{1}{\sqrt{\tilde{a}_{ii}}}$.

A special band storage scheme was implemented to use the sparse structure of the symmetric matrix in the system [37].

3.7 Description of the incremental model for large deformations

The developed linear approach assumes that only small displacements occur as a result of deformation. To overcome this limitation, we use the Lagrangian incremental method [13], [41]. The idea of incremental methods is to let the applied forces vary by small increments, so the non-linear solution is approximated by successively solving corresponding linear problems.

Starting from $\mathbf{u}^0 = \mathbf{0}$, two arbitrary steps of the incremental process can be written as:

$$\begin{aligned} \mathbf{A}(\mathbf{u}^n) &= \mathbf{f}^n, \\ \mathbf{A}(\mathbf{u}^{n+1}) &= \mathbf{f}^{n+1}, \end{aligned} \tag{32}$$

where $\mathbf{A}$ is the non-linear elasticity operator introduced in (9).

We define the n-th force and displacement increments as:

$$\begin{aligned} \boldsymbol{\delta}\mathbf{f}^n &= \mathbf{f}^{n+1} - \mathbf{f}^n = \mathbf{A}(\mathbf{u}^{n+1}) - \mathbf{A}(\mathbf{u}^n), \\ \boldsymbol{\delta}\mathbf{u}^n &= \mathbf{u}^{n+1} - \mathbf{u}^n. \end{aligned} \tag{33}$$

But since

$$\mathbf{A}(\mathbf{u}^{n+1}) - \mathbf{A}(\mathbf{u}^n) = \mathbf{A}'(\mathbf{u}^n)(\mathbf{u}^{n+1} - \mathbf{u}^n) + o(\mathbf{u}^{n+1} - \mathbf{u}^n), \tag{34}$$

the incremental method can be formulated as linear approximation of (34):

$$\mathbf{A}'(\mathbf{u}^n)\boldsymbol{\delta}\mathbf{u}^n = \boldsymbol{\delta}\mathbf{f}^n. \tag{35}$$

In contrast, the linearized problem, defined as

$$\mathbf{A}'(\mathbf{0})\mathbf{u} = \mathbf{f}, \tag{36}$$

assumes only small strains and is not suitable for computations of large deformations.

The formulation (35) is similar to the traditional *Newton's method* [28] of solving non-linear equations which can also be applied for linearization of the registration model (9). However, it is known for Newton's method that its convergence generally strongly depends on the optimal choice of the start value $\mathbf{u}^0$.

The existence result and the proof of the convergence of the incremental method (35) can be found in [13].

FEM discretization of the incremental model

The term $\mathbf{A}'(\mathbf{u}^n)\boldsymbol{\delta}\mathbf{u}^n$ in (35) with the parameter λ excluded is given as [13]

$$\mathbf{A}_i'(\mathbf{u}^n)\boldsymbol{\delta}\mathbf{u}^n = -\sum_{j,p,q=1}^{3} \partial_j(\hat{a}_{ijpq}(\boldsymbol{\nabla}\mathbf{u}^n)\partial_p \delta u_q^n), \tag{37}$$

where

$$\begin{aligned}\hat{a}_{ijpq}(\boldsymbol{\nabla}\mathbf{u}^n) = a_{ijpq} + \sum_{k=1}^{3} a_{kjpq}\partial_k u_i^n +& \\ \sum_{r=1}^{3} a_{ijrp}\partial_r u_q^n + + \sum_{k,r=1}^{3} a_{kjpr}\partial_r u_q^n \partial_k u_i^n +& \\ \sum_{s,r=1}^{3} a_{pjsr}E_{sr}(\mathbf{u}^n)\delta_{iq}.&\end{aligned} \tag{38}$$

Here, $a_{ijpq} = \frac{1}{2}(\delta_{ip}\delta_{jq} + \delta_{iq}\delta_{jp})$, $i, j, p, q = 1, 2, 3$, and E_{sr} denote the components of the Green-St. Venant strain tensor (4).

The variational formulation of (35) can now be written as

$$\int_\Omega \sum_{j,p,q=1}^{3} \hat{a}_{ijpq}(\boldsymbol{\nabla}\mathbf{u}^n)\partial_p \delta u_q^n \partial_j v_i \, dx = \frac{1}{\mu}\int_\Omega \delta f_i^n v_i \, dx; \quad i = 1, 2, 3, \tag{39}$$

where $\mathbf{v} \in \mathbf{V}$ are test functions.

Analogously to the linear model in Section 3.3, we replace the space $\mathbf{V}$ with a finite-dimensional subspace $\mathbf{V}_N \subset \mathbf{V}$ and represent the functions $\mathbf{u}_N^n$, $\mathbf{v}_N$, $\boldsymbol{\delta}\mathbf{u}_N^n \in \mathbf{V}_N$ as finite weighted sums of basis functions. We then obtain the solution vector $\boldsymbol{\delta}\mathbf{u}^n = \{\delta u_i^n\}$ as a solution of the following linear system of Galerkin equations:

$$\sum_{k=1}^{N} \delta u_k^n \int_\Omega \sum_{i,j,p,q=1}^{3} \hat{a}_{ijpq}(\boldsymbol{\phi}^n)\partial_p \phi_k \partial_j \phi_l \, dx = \frac{1}{\mu}\int_\Omega \boldsymbol{\delta}\mathbf{f}^n \cdot \boldsymbol{\phi}_l \, dx; \quad l = 1, \ldots, N, \tag{40}$$

where $\hat{a}_{ijpq}(\boldsymbol{\phi}^n)$ denotes the FEM discretization of (38).

Parameter-free formulation of the incremental method can be obtained analogously to the linear model.

Discrete solution

When applying the incremental method implemented on a discrete grid in the case of large deformations, after some iterations the deformation gradient locally approaches zero due to discretization. As a consequence, the stiffness matrix of the incremental method becomes badly conditioned and its further updates are not possible.

One possibility to obviate this problem is to use the *propagation of templates* [10]: If the deformation gradient is close to zero, the deformation $\boldsymbol{\phi}^1(\mathbf{x}) = \mathbf{x} + \mathbf{u}^i$ is computed, $\mathbf{u}^i$ is set

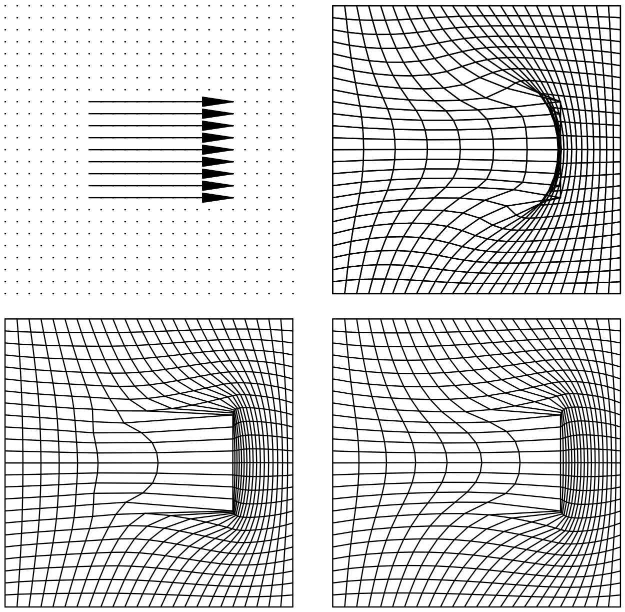

Figure 3: Deformation with large displacements. Top row/left: Prescribed displacements. Top row/right: Deformation computed with the linear model. Bottom row: Deformation computed with the incremental model with memory (left) and without memory (right). One can see that the incremental model preserves the topology when computing large deformations.

to zero and a new iteration process is started with a new template. We compute in the similar way the deformation $\boldsymbol{\phi}^2(\mathbf{x}) = \boldsymbol{\phi}^1(\mathbf{x}) + \mathbf{u}^i$, etc. The resulting deformation $\boldsymbol{\phi}$ is obtained as a composition of k iteration processes

$$\boldsymbol{\phi} = \boldsymbol{\phi}^k \circ \boldsymbol{\phi}^{k-1} \circ \ldots \circ \boldsymbol{\phi}^1. \tag{41}$$

The drawback of this scheme is that a new template is used with each new iteration process. As a consequence, we may obtain unrealistic resulting deformations.

Another method is to use approximations of $\mathbf{A}'(\mathbf{u}^n)$ in the iteration process. One approximation can be obtained as:

$$\mathbf{A}'(\mathbf{u}^n) \approx \mathbf{A}'(\mathbf{u}^k), \qquad k = \max\{i \in \{0, \ldots, n\} \,|\, \det(\mathbf{I} + \boldsymbol{\nabla}\mathbf{u}^i) \geq \epsilon\}. \tag{42}$$

In other words, we do not compute the update of the stiffness matrix if the determinant of the Jacobian of the deformation field falls lower than ϵ. In this case, we preserve memory about several preceding deformations. This scheme is analogous to the combination of Newton's method with the *chord method* [28] for solving non-linear equations.

Another possibility to approximate $\mathbf{A}'(\mathbf{u}^n)$ is, analogously to the chord method, to take $\mathbf{A}'(\mathbf{u}^0) = \mathbf{A}'(\mathbf{0})$ as an approximation of $\mathbf{A}'(\mathbf{u}^n)$. This means that we do not carry memory about preceding deformations in our model. An advantage is that this method is less computationally expensive compared to the previous one.

In the experiment presented below, we have investigated the latter two approximations of $\mathbf{A}'(\mathbf{u}^n)$.

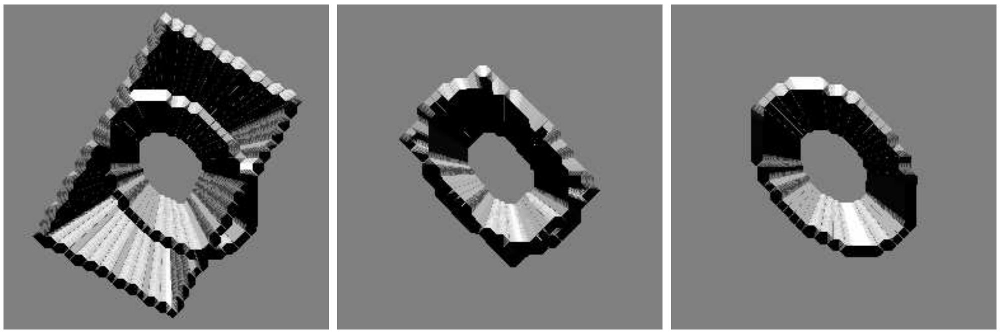

Figure 4: Registration of 3-D synthetic images. Left: Superimposed original images. Middle: Principal axes transformation applied to the box. Right: Result of the elastic registration. Compared to the image in the middle, the correspondence between boundaries of the source and target image is more accurate.

4 Experiments

In this section, we present experimental results with our approach. In all experiments, the Lagrangian reference frame has been used [29], where the position of a point in the deformed image is obtained as a sum of its position in the source image and the computed displacement. The incremental model has been used in the first experiment for comparison with the linear model. In all other experiments, we have used the linear model, since it has provided satisfactory registration results.

In the first experiment, a deformation with large prescribed displacements was performed on a 25x25 rectangular grid (Figure 3). We prescribed displacements of 12 pixels in the middle of the grid (Figure 3/top row/left), so the local horizontal expansion was almost equal to the half of the image dimension. The result of the application of the linear model is shown in the right image in the top row of the figure. As one can see, the resulting deformation does not preserve the topology, since the linear elastic model is not suitable for computations of large deformations. In the bottom row of Figure 3, the deformations computed due to the incremental model are shown. In the left image, the result of the application of the incremental model with memory is depicted. The value of ϵ for this experiment has been set to 0.2. In the right image, the deformation computed with the incremental model without memory is presented. We can see that both incrementally computed deformations preserve the topology but the deformation with memory is less smooth.

In our next experiment, two synthetic 3-D images of size 64x64x30 have been registered (Figure 4). We first applied a principal axes transformation to the box (Figure 4/middle) and then elastically deformed it by using the linear elastic model to register it with the 3-D ellipse (Figure 4/right). The prescribed displacements for this experiment have been obtained by using the 3-D minimal distance algorithm. After elastic transformation, the boundary of the box accurately matches to the boundary of the ellipse.

In the next experiment, we register two 2-D MR brain images (256x256) taken from different patients (top row of Figure 5), where the skull has been manually removed. Note, that the two images differ significantly in overall shape. The principal axes transformation was applied to the source image (top row/left) to correct translational, rotational, and scaling differences. The result is shown in the left image in the bottom row of the figure. The outer contour of the transformed source image was next mapped to the outer contour of the target image by using the minimal distance algorithm. The displacements obtained by this mapping were then used as constraints in the linear elastic deformation model using bilinear interpolation applied in the following step to compensate discretization effects (bottom row/right). One can see that a good correspondence of the outer contours of the source and target image has been obtained after elastic transformation.

Figure 6 illustrates in more detail the preservation of prescribed displacements in the elastic deformation example from the previous experiment (Figure 5). In the figure, an enlarged 20x20 section of the lower left part of the image before elastic registration, the prescribed displacements, and the displacements computed as a result of elastic deformation are shown. The vector fields have been scaled for better visibility.

In Figure 7, we present an alternative way of defining points correspondences required for registration. For this experiment, we used the snake model for segmentation of the outer contour and of the boundaries of the ventricles from the source image (after translational and scaling correction) and from the target one. The initial and final position of the snakes on the globally transformed source image are shown in the middle row of Figure 7. The correspondences obtained from the converged curves were next used to perform the elastic registration. The source image before and after the elastic registration with the superimposed contours of the target image is shown in the bottom row of Figure 7. A rather good registration of the outer contours and of the ventricle system was reached in spite of considerable differences in the images prior to the elastic transformation. One can also see that the snake model did not provide correct correspondences for the lower part of the slice because of the significant difference in shape between the source and target image. As a consequence, the lower part of the resulting image is somewhat skewed.

In a further experiment, we matched a 3-D synthetic image with a part of the cortical surface. The cortical boundary was extracted by simply applying an edge detector to each slice of the brain image. The cube was then elastically deformed by using the linear model with prescribed displacements obtained with the help of the 3-D minimal distance algorithm. The size of both images was 80x80x80 voxels.

The result of the experiment is presented in the top row of Figure 8, where the 3-D renderings of the outer contours of the source, target, and deformed source image are shown. Despite the complicated shape of the cortical surface, a rather good approximation of it has been obtained.

In the middle row of Figure 8, the magnitudes of the displacement field are shown for the slices 15, 30, 45. To be more illustrative, the magnitudes of $\mathbf{u}(\mathbf{x})$ are shown at the points $\mathbf{x} + \mathbf{u}(\mathbf{x})$. In the bottom row, the deformations of the slices 15, 30, 45 are represented as deformations of a rectangular grid.

In our last experiment, 8 contiguous slices from a 3-D MR data set have been matched to eight corresponding slices taken from a digital atlas of brain anatomy. For the experiment, we selected the slices from the data set where the ventricle system well corresponded to that of the atlas. The brain was extracted from the data set by component labeling of the thresholded data. The threshold was chosen to allow the sufficient smoothing of the cortical boundary, this is important for correctly mapping cortical boundaries using the minimal distance algorithm. Again, we used our approach to refine a global transformation of the original image.

In Figure 9, one slice from the original data set (left), the result of the thresholding operation applied to the slice (middle), and the extracted brain slice (right) are shown.

As a global transformation for comparison purposes, a thin-plate spline transformation [34] with 15 pairs of point landmarks, which have been manually localized, was applied to the extracted brain image to match it with the digital atlas. Note, that this transformation already represents elastic deformations. The landmarks have been distributed within the 8 slices and are located at the ventricle horns, the corpus callosum, and the outer brain contours. The boundaries of the cortex and the ventricles were further mapped to the manually smoothed

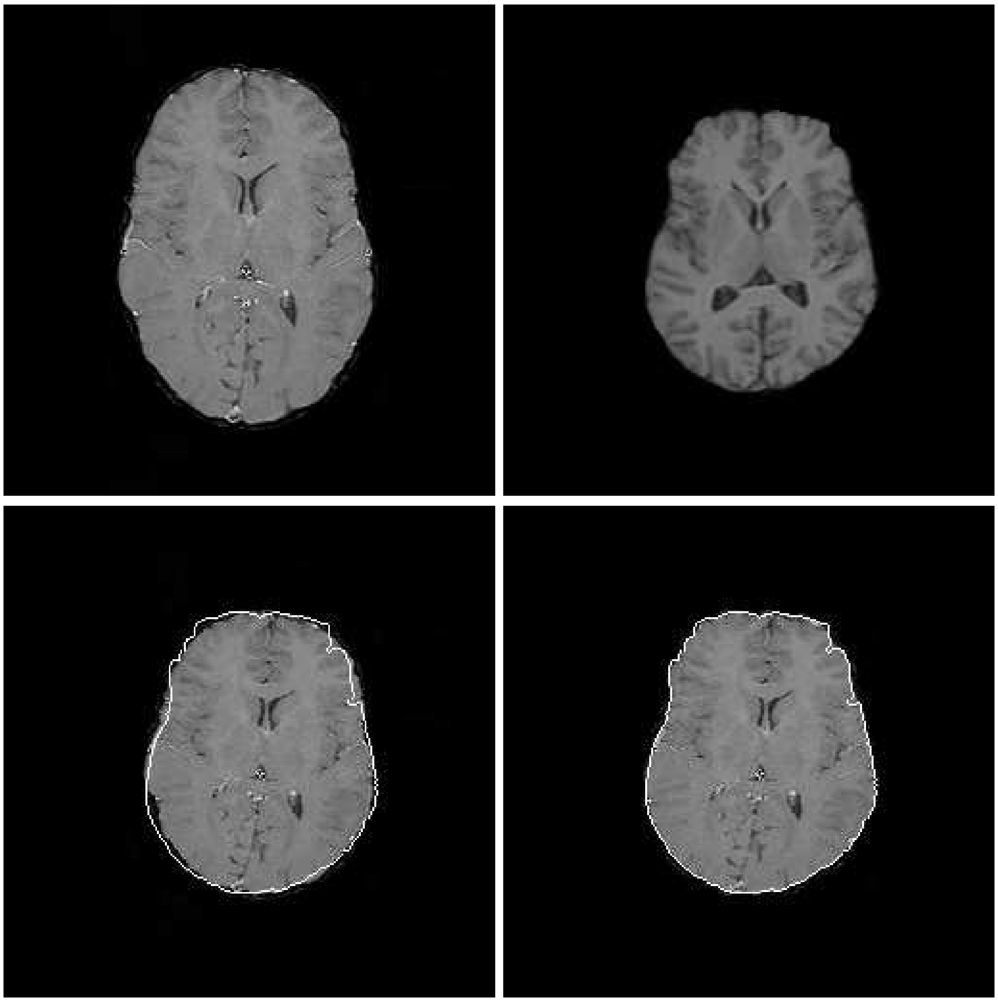

Figure 5: 2-D registration example. Top row: Two MR slices taken from different patients with the source image at the left. Bottom row/left: Principal axes transformation applied to the source image with the superimposed outer contour of the target image. Bottom row/right: Elastic registration of the transformed source image. Compared to the global transformation, the correspondence between boundaries of the source and target image is more accurate.

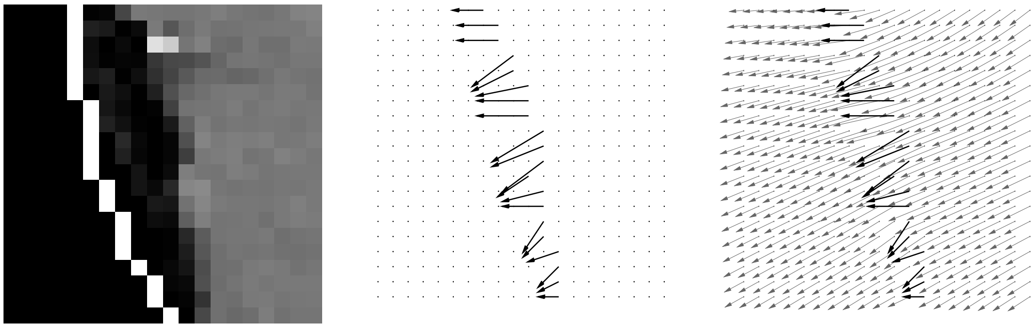

Figure 6: Vector fields of prescribed displacements (middle) and displacements computed as a result of elastic deformation (right) for the 2-D registration experiment in Figure 5.

cortical boundary and to the ventricles of the atlas by using the 3-D minimal distance algorithm. The obtained displacements were then used for the linear elastic deformation of the globally transformed image. In order to apply the homogeneous Dirichlet boundary conditions, ten empty slices were added to the each side of the image and to the part of the atlas in order to exclude contact of the brain to the image boundary, so the total dimensions of the images in the experiment were 90x116x28 voxels. The elastically deformed image was trilinearly interpolated to cope with discontinuities due to discretization.

In Figure 10, the original 3-D image with superimposed atlas contours (left), the thin-plate spline transformation of the original image (middle) and the elastic registration of the transformed image are presented. For illustration purposes, enlarged 2-D sections of the image after thin-plate spline and elastic transformation are shown in Figure 11.

The 3-D minimal distance algorithm which was used to obtain prescribed displacements is well suited to match overlapping smooth surfaces, so a quite good refinement was achieved in this experiment along the cortical boundary. Because of the complicated 3-D shape of the ventricles, the minimal distance algorithm is generally not suited to obtain correspondences for the ventricle system in 3-D. As a consequence, almost no improvements were achieved by additionally matching the ventricle system in contrast to the 2-D experiment in Figure 7, since no appropriate input data were available.

5 Discussion

We have presented a parameter-free registration approach where images are elastically deformed through incorporation of prescribed displacements obtained by mapping boundary structures. The desired global mapping of the source image onto the target one is constrained by using local values of this mapping (known displacements of boundary structures). In contrast to traditional methods, our approach does not depend on parameters of the deformation model such as elastic constants. The approach guarantees the *exact* matching of boundary structures if the correct input data are available. Driving forces are *implicitly* incorporated in the model and can be restored by using the inverse of (17) [30].

The presented linear model is closely related to that in [20], [18] which can produce similar results by assigning sufficiently small values to the model parameters (elastic constants) and which then also becomes parameter-free in the limit. However, the drawback of the formulation in [20], [18] is that the involved stiffness matrix may be badly conditioned because of too small parameter values. To illustrate this, the dependence of the condition number $k(A)$ of the

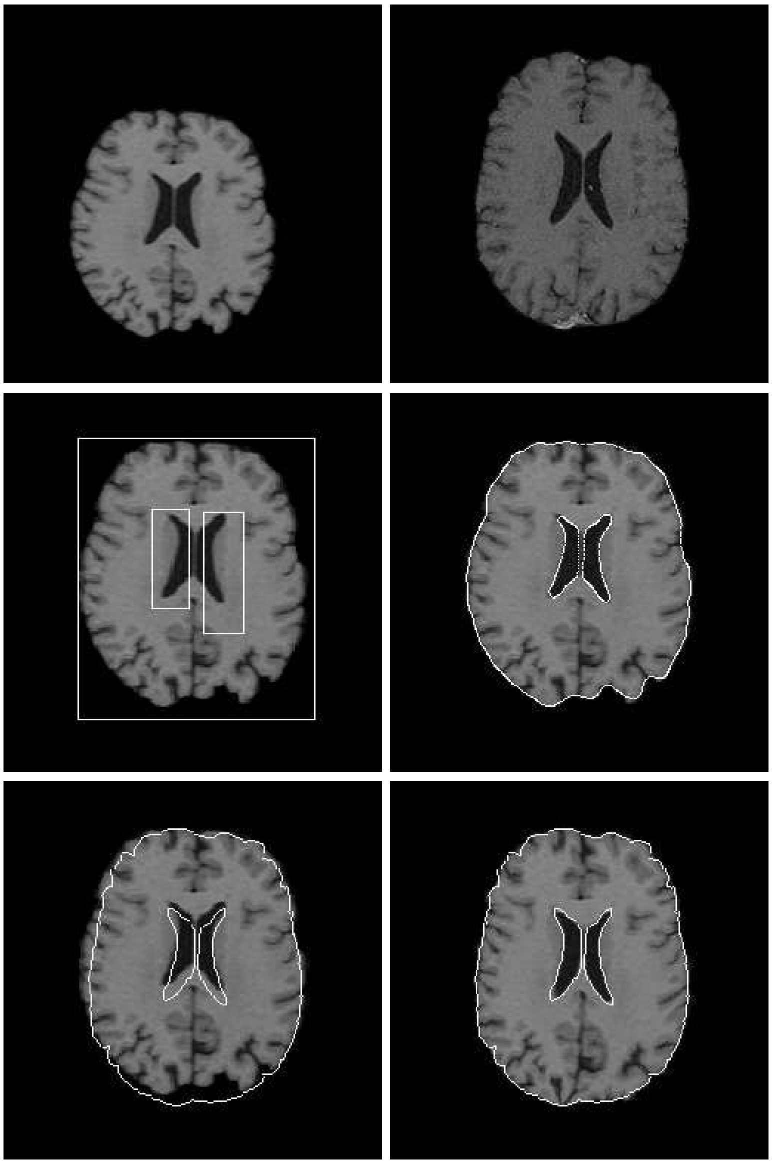

Figure 7: 2-D registration example. Top row: Two MR slices taken from different patients with the source image at the left. Middle row: Initial and final position of the snakes on the globally transformed source image. Bottom row/left: Globally transformed source image with the superimposed contours from the target image. Bottom row/right: Result of elastic registration. Good registration of the outer contours and of the ventricle system has been obtained in comparison to the global transformation.

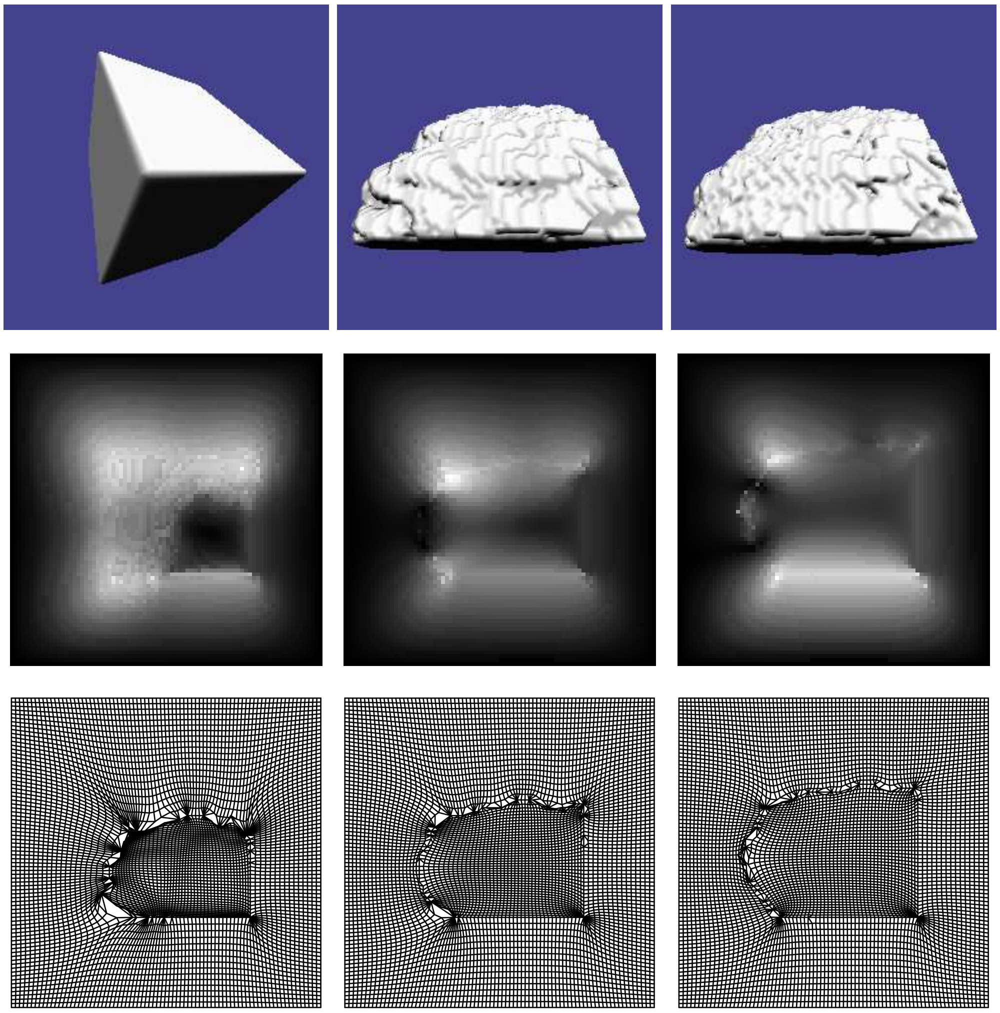

Figure 8: 3-D registration experiment. Top row: Source, target, and deformed source image. Middle row: Magnitudes of the displacement field for the horizontal slices 15, 30, 45. Bottom row: Deformations of the horizontal slices 15, 30, 45 projected onto the xy-plane.

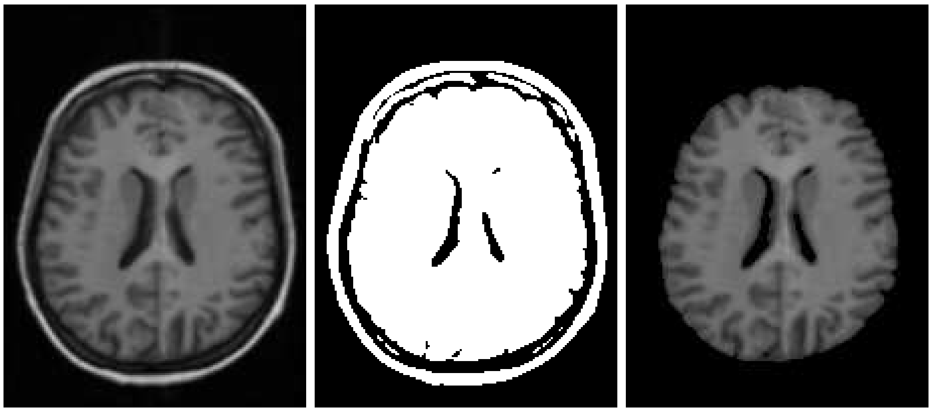

Figure 9: Left: One slice from the original 3-D MR data set. Middle: Result of the thresholding operation applied to the slice. Right: Extracted brain. The segmented brain has then been used as input data for the experiment presented in Figure 10.

Figure 10: Left: The original 3-D image with atlas contours superimposed. Middle: Thin-plate spline transformation of the original image. Right: Elastic registration of the transformed image.

stiffness matrix on m, where $\mu = 10^{-m}$, for the linear model developed in [20], [18], is shown in Figure 12. For comparison, the condition number of the matrix corresponding to the model developed in this paper is shown as a dashed line. The stiffness matrix was taken from the experiment presented in Figure 3, and the parameter λ in the model from [20], [18] was set to zero for compatibility with the model presented herein. Taking into account that the condition number also strongly depends on image dimensions, the method developed in [20], [18] can be numerically unstable for large-sized 3-D problems, especially in the case of parallel realization. The reason is that efficient preconditioners such as incomplete LU factorization can hardly be used in parallel realizations. As a consequence, a badly conditioned model may require more iteration steps to obtain the solution. In contrast, the model presented in this paper exactly preserves the boundary mapping independently from the parameter values and is well conditioned.

We have also applied the Lagrangian incremental method to cope with *large* deformations. It is computationally expensive, since in each iteration step a complete linear problem must be solved but, on the other side, it helps to prevent topology violations while computing large deformations. From the experimental results, we could conclude that the incremental method without memory produced more smooth deformations compared to the method where the memory about several preceding steps was preserved.

An important point is the efficient numerical implementation of the approach. The extremely high number of variables of the deformation model in the 3-D case requires large amounts of memory. Since the stiffness matrix requires modification, it cannot simply be inverted for fixed image dimensions, and iterative algorithms need to be used. The implemented method of conjugate gradients with preconditioning shows quite acceptable results if the matrix can completely be loaded into the computer memory (the registration of a 80x80x80 image took about 23 minutes on an SGI Power Challenge). But for the usage of our approach in real medical applications, further development using explicit parallelization (and possibly multi-grid techniques) is required.

One aspect of future research is the derivation of practically applicable methods for obtaining point correspondences between boundary structures in the image. There are generally two possibilities to obtain such correspondences, both of them having their advantages and drawbacks: The usage of active surfaces or the mapping of segmented boundaries (see also Section 3.4). In the present paper, we used the snake model and the minimal distance algorithm to obtain point correspondences between boundary structures in the brain. Since anatomic structures of the brain can have very complicated shapes, more sophisticated surface matching techniques, for example based on the shape modeling, are required.

Another important problem, which requires further investigation, is the derivation of a reliable criterion to determine the exact application scope of the linear model, since it is less computationally expensive compared to the incremental model.

Acknowledgements

The first author would like to thank the German Academic Exchange Service (DAAD) for support. Medical image data were provided by R. Shahidi, the UMDS Image Processing Group (London/UK), Philips Research Laboratories Hamburg, and University Hospital Eppendorf (UKE), Hamburg. The atlas of brain anatomy was kindly provided by Dr. F.-J. Schuier of Dept. of Neurology, Rheinische Landes- und Hochschulklinik Düsseldorf.

The authors also would like to thank the anonymous reviewers for their constructive comments on this paper.

A Notation

$\mathbb{R}$ - space of real numbers
$\mathbb{R}^{n\times n}$ - space of real square matrices of order n
$\mathbf{e}_1, \mathbf{e}_2, \ldots, \mathbf{e}_n$ - basis vectors in $\mathbb{R}^n$
Ω - bounded open subset of $\mathbb{R}^n$
$\bar{\Omega}$ - closure of the set Ω
Γ - boundary of the set Ω
Γ_1 - subset of Γ
$\emptyset$ - empty set
$\partial_i = \partial/\partial x_i$ - partial derivative with respect to x_i
∂^{α} - partial derivative of order α
$\mathbf{u}\cdot\mathbf{v} = \mathbf{u}^{\mathrm{T}}\mathbf{v}$ - vector inner product
$\det(\mathbf{A})$ - determinant of a matrix
$\mathrm{tr}(\mathbf{A}) = \sum_i a_{ii}$ - trace of a matrix

$\langle \mathbf{A}, \mathbf{B} \rangle = \mathrm{tr}(\mathbf{A}^{\mathrm{T}}\mathbf{B})$ - usual matrix inner product
$\mathbf{div}\, \mathbf{T} = \sum_i \sum_j \partial_j T_{ij} \mathbf{e}_i$ - divergence of a tensor field
$L^2(\Omega)$ - space of quadratic-integrable functions on Ω
$H^m(\Omega)$ - Sobolev spaces, $m = 1, 2, \ldots$
$||\cdot||$ - norm in a vector space
$||\cdot||_{m,\Omega}$ - norm in a Sobolev space $H^m(\Omega)$, $||v||_{m,\,\Omega} = \left\{ \int_\Omega \sum_{|\alpha| \le m} |\partial^{\,\alpha} v|^2 \, dx \right\}^{1/2}$, $|\alpha| = \sum_{i=1}^n \alpha_i$

B Existence and uniqueness of the solution for the linear model

In the following, we explicitly outline the existence theory for the variational formulation (14).

We have the following variational problem: Find $\mathbf{u} \in \mathbf{V}$ such that

$$a(\mathbf{u}, \mathbf{v}) = l(\mathbf{v}), \quad \forall \mathbf{v} \in \mathbf{V}, \tag{43}$$

where:

$$a(\mathbf{u}, \mathbf{v}) = \int_\Omega \langle \mathbf{e}(\mathbf{u}), \mathbf{e}(\mathbf{v}) \rangle \, dx, \tag{44}$$

$$l(\mathbf{v}) = \frac{1}{2\mu} \int_\Omega \mathbf{f} \cdot \mathbf{v} \, dx. \tag{45}$$

To show that this problem has a unique solution, we first cite the following theorem [13]:

Theorem 1 *Let $\mathbf{V}$ be a Banach space with norm $||\cdot||$, let $l : \mathbf{V} \longrightarrow \mathbb{R}$ be a continuous linear form, and let $a(\cdot\,,\cdot) : \mathbf{V} \times \mathbf{V} \longrightarrow \mathbb{R}$ be a symmetric continuous $\mathbf{V}$-elliptic bilinear form in the sense that there exists a constant β such that*

$$\beta > 0 \text{ and } a(\mathbf{v}, \mathbf{v}) \ge \beta ||\mathbf{v}||^2, \quad \forall \mathbf{v} \in \mathbf{V}.$$

Then the variational problem: Find $\mathbf{u} \in \mathbf{V}$ such that

$$a(\mathbf{u}, \mathbf{v}) = l(\mathbf{v}), \quad \forall \mathbf{v} \in \mathbf{V},$$

has one and only one solution. □

By using the Cauchy-Schwarz inequality, one can show that both forms in (43) are bounded with respect to the norm $||\cdot||_{1,\Omega}$ and, consequently, are continuous over the space $\mathbf{V}$ [8].

The bilinear form $a(\mathbf{u}, \mathbf{v})$ in (43) is bounded, since

$$||a(\mathbf{u}, \mathbf{v})|| \le ||\mathbf{e}(\mathbf{u})||_{0,\Omega} ||\mathbf{e}(\mathbf{v})||_{0,\Omega}, \tag{46}$$

and continuous, since the norm $||\mathbf{e}(\mathbf{v})||_{0,\Omega}$ is equivalent to the norm $||\cdot||_{1,\Omega}$, as it will be shown below.

Analogously, the linear form $l(\mathbf{v})$ in (43) is continuous, since

$$||l(\mathbf{v})|| \le C_\mu ||\mathbf{f}||_{0,\Omega} ||\mathbf{v}||_{0,\Omega} \le C_\mu ||\mathbf{f}||_{0,\Omega} ||\mathbf{v}||_{1,\Omega}, \tag{47}$$

where $C_\mu = \frac{1}{2\mu}$.

The $\mathbf{V}$-ellipticity of (44) can be shown by proving that the norm

$$||\mathbf{e}(\mathbf{v})||_{0,\Omega} = \left\{ \int_\Omega \langle \mathbf{e}(\mathbf{v}), \mathbf{e}(\mathbf{v}) \rangle \, dx \right\}^{1/2} \tag{48}$$

is equivalent to the norm $||\cdot||_{1,\Omega}$.

This can be done by using Korn's inequality: There exists a constant c such that

$$||\mathbf{v}||_{1,\Omega} \leq c\,(||\mathbf{v}||^2_{0,\Omega} + ||\mathbf{e}(\mathbf{v})||^2_{0,\Omega})^{1/2}, \qquad \forall \mathbf{v} \in (H^1(\Omega))^3. \quad (49)$$

With this inequality, one can show that the mapping

$$\mathbf{v} \longrightarrow (||\mathbf{v}||^2_{0,\Omega} + ||\mathbf{e}(\mathbf{v})||^2_{0,\Omega})^{1/2} \quad (50)$$

is a norm over the space $\mathbf{V}$ equivalent to the norm $||\cdot||_{1,\Omega}$ and, consequently ([13], Theorem 6.3-4),

$$c^{-1}||\mathbf{v}||_{1,\Omega} \leq ||\mathbf{e}(\mathbf{v})||_{0,\Omega} \leq c||\mathbf{v}||_{1,\Omega}, \ \forall \mathbf{v} \in \mathbf{V}, \quad (51)$$

so the two norms in (51) are equivalent.

Therefore we have

$$a(\mathbf{v}, \mathbf{v}) = ||\mathbf{e}(\mathbf{v})||^2_{0,\Omega}, \quad (52)$$

and the bilinear form (44) is $\mathbf{V}$-elliptic.

References

[1] A.A. Amini, R.L. Owen, P. Anandan, and J.S. Duncan. Non-rigid motion models for tracking the left-ventricular wall. In *Lecture Note in Computer Science: Information Processing in Medical Images*, pages 343–356. Springer-Verlag, 1991.

[2] R. Bajcsy and S. Kovačič. Multiresolution elastic matching. *Computer Vision, Graphics, and Image Processing*, 46:1–21, 1989.

[3] P.J. Besl and N.D. McKay. A method for registration of 3-D shapes. *IEEE Transactions on Pattern Analysis and Machine Intelligence*, 14(2):239–256, 1992.

[4] F.L. Bookstein. Principal warps: Thin-plate splines and the decomposition of deformations. *IEEE Transactions on Pattern Analysis and Machine Intelligence*, 11(6):567–585, 1989.

[5] M. Bro-Nielsen. *Medical Image Registration and Surgery Simulation.* PhD thesis, Technical University of Denmark, August 1996.

[6] M. Bro-Nielsen and C. Gramkow. Fast fluid registration of medical images. In *Proc. Visualization in Biomedical Computing (VBC'96)*, volume 1131 of *Lecture Notes in Computer Science*, pages 267–276, Hamburg, Germany, September 1996. Springer-Verlag.

[7] C. Broit. *Optimal Registration of Deformed Images.* Doctoral dissertation, University of Pennsylvania, August 1981.

[8] K. Burg, H. Haf, and F. Wille. *Höhere Mathematik für Ingenieure*, volume V. Teubner, Stuttgart, 1991.

[9] V. Caselles, F. Catte, T. Coll, and F. Dibos. A geometric model for active contours. *Numerische Mathematik*, 66:1–31, 1993.

[10] G.E. Christensen. *Deformable Shape Models for Anatomy.* Doctoral dissertation, Washington University, August 1994.

[11] G.E. Christensen, R.D. Rabbitt, and M.I. Miller. Deformable templates using large deformation kinematics. *IEEE Transactions on Image Processing*, 5(10):1435–1447, 1996.

[12] P.G. Ciarlet. *The Finite Element Method for Elliptic Problems*, volume 4 of *Studies in Mathematics and its Applications*. North-Holland, Amsterdam, 1978.

[13] P.G. Ciarlet. *Mathematical Elasticity. Volume I: Three-Dimensional Elasticity*, volume 20 of *Studies in Mathematics and its Applications*. North-Holland, Amsterdam, 1988.

[14] L.D. Cohen. Auxiliary variables and two-step iterative algorithms in computer vision problems. *Journal of Mathematical Imaging and Vision*, 6:59–83, 1996.

[15] L.D. Cohen and I. Cohen. Finite-element-methods for active contour models and balloons for 2-D and 3-D images. *IEEE Transactions on Pattern Analysis and Machine Intelligence*, 15(11):1131–1147, 1993.

[16] A. Collignon, F. Maes, D. Delaere, D. Vandermeulen, P. Suetens, and G. Marchal. Automated multi-modality image registration based on information theory. In *Proc. 14th International Conference on Information Processing in Medical Imaging*, pages 263–274, Ile de Berder, France, June 1995. Kluwer Academic Publishers.

[17] C. Cuvelier, A. Segal, and A.A. van Steenhoven. *Finite Element Methods and Navier-Stokes Equations*. D. Reidel Publishing Co., Dordrecht, Holland, 1986.

[18] C. Davatzikos. Spatial transformation and registration of brain images using elastically deformable models. *Computer Vision and Image Understanding, Special Issue on Medical Imaging*, 66(2):207–222, 1997.

[19] C. Davatzikos and R.N. Bryan. Using a deformable model to obtain a shape representation of the cortex. *IEEE Transactions on Medical Imaging*, 15:785–795, 1996.

[20] C. Davatzikos, J.L. Prince, and R.N. Bryan. Image registration based on boundary mapping. *IEEE Transactions on Medical Imaging*, 15(1):112–115, 1996.

[21] M.H. Davis, A. Khotanzad, D.P. Flaming, and S.E. Harms. A physics-based coordinate transform for 3-D image matching. *IEEE Transactions on Medical Imaging*, 16(3):317–328, June 1997.

[22] P.A. van den Elsen, J.B.A. Maintz, E.-J.D. Pol, and M.A. Viergever. Automatic registration of CT and MR brain images using correlation of geometrical features. *IEEE Transactions on Medical Imaging*, 14(2):384–396, 1995.

[23] G. Fischer. *Lineare Algebra*. Vieweg, Braunschweig, 1986.

[24] J.C. Gee, D.R. Haynor, M. Reivich, and R. Bajcsy. Finite element approach to warping brain images. In *Proc. SPIE Image Processing*, volume 2167, pages 327–337, 1994.

[25] W. Hackbusch. *Iterative Solution of Large Sparse Systems of Equations*. Springer-Verlag, 1993.

[26] C. Kambhamettu and D. Goldgof. Curvature-based approach to point correspondence recovery in conformal non-rigid motion. *CVGIP: Image Understanding*, 60(1):26–43, 1994.

[27] M. Kass, A. Witkin, and D. Terzopoulos. Snakes: Active contour models. *International Journal of Computer Vision*, 1(4):321–331, 1988.

[28] C.T. Kelley. *Iterative Methods for Linear and Nonlinear Equations.* SIAM, Philadelphia, 1995.

[29] L.E. Malvern. *Introduction to the Mechanics of a Continuous Medium.* Prentice-Hall, 1969.

[30] W. Peckar. FEM dicretization of the Navier equation with applications to medical imaging. Memo FBI-HH-M-266/96, Dept. of Computer Science, University of Hamburg, November 1996.

[31] W. Peckar, C. Schnörr, K. Rohr, and H.S. Stiehl. Two-step parameter-free elastic image registration with prescribed point displacements. In *Proc. 9th Int. Conf. on Image Analysis and Processing (ICIAP '97)*, volume 1310 of *Lecture Notes in Computer Science*, pages 527–534, Florence, Italy, September 1997. Springer-Verlag.

[32] C.A. Pelizarri, G.T.Y. Chen, D.R. Spelbring, R.R. Weichselbaum, and C.-T. Chen. Accurate three-dimensional registration of CT, PET, and/or MR images of the brain. *Journal of Computer Assisted Tomography*, 13(1):20–26, 1989.

[33] R.D. Rabbitt, J.A. Weiss, G.E. Christensen, and M.I. Miller. Mapping of hyperelastic deformable templates using the finite element method. In *Proc. SPIE Vision Geometry IV*, volume 2573, pages 252–265, 1995.

[34] K. Rohr, H.S. Stiehl, R. Sprengel, W. Beil, T.M. Buzug, J. Weese, and M.H. Kuhn. Point-based elastic registration of medical image data using approximating thin-plate splines. In *Proc. Visualization in Biomedical Computing (VBC'96)*, volume 1131 of *Lecture Notes in Computer Science*, pages 297–306, Hamburg, Germany, September 1996. Springer-Verlag.

[35] S. Sandor and R. Leahy. Surface-based labeling of cortical anatomy using a deformable atlas. *IEEE Transactions on Medical Imaging*, 16(1):41–54, 1997.

[36] T. Schormann, S. Henn, and K. Zilles. A new approach to fast elastic alignment with applications to human brains. In *Proc. Visualization in Biomedical Computing (VBC'96)*, volume 1131 of *Lecture Notes in Computer Science*, pages 337–342, Hamburg, Germany, September 1996. Springer-Verlag.

[37] H.R. Schwarz. *Methode der finiten Elemente.* Teubner, Stuttgart, 1984.

[38] J. Shen and S. Castan. An optimal linear operator for edge detection. In *Proc. IEEE Conf. on Computer Vision and Pattern Recognition (CVPR'86)*, pages 109–114, Miami, June 1986.

[39] R. Szeliski and S. Lavallée. Matching 3-D anatomical surfaces with non-rigid deformations using octree-splines. *International Journal of Computer Vision*, 18(2):171–186, 1996.

[40] P. Thompson and A. Toga. A surface-based technique for warping three-dimensional images of the brain. *IEEE Transactions on Medical Imaging*, 15(4):401–417, 1996.

[41] K. Washizu. *Variational Methods in Elasticity and Plasticity.* Pergamon Press, Oxford, second edition, 1982.

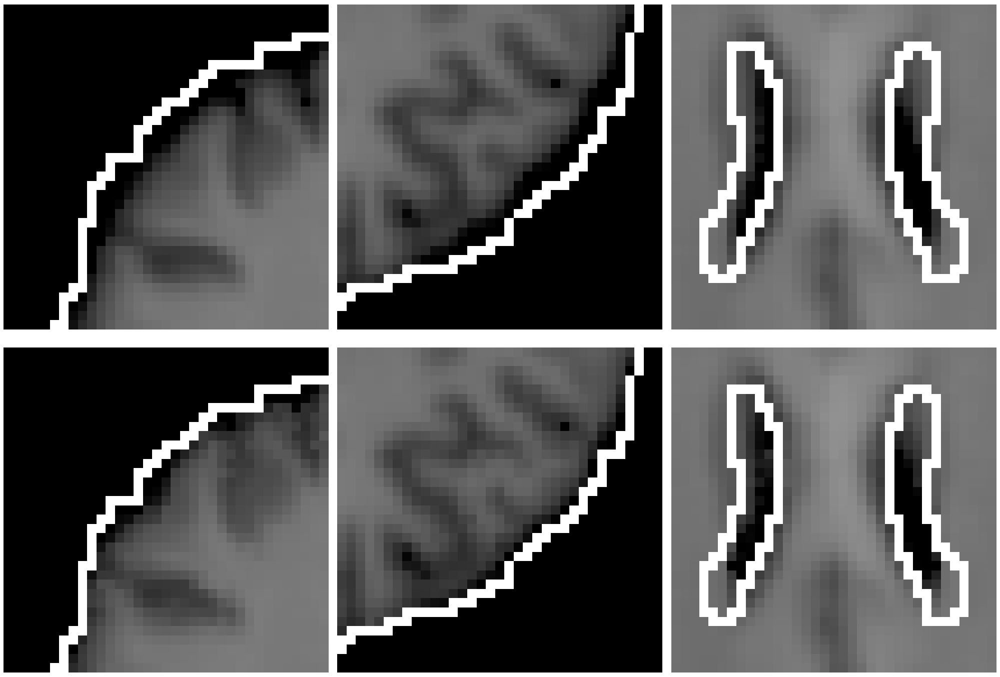

Figure 11: Enlarged sections from the 3-D matching experiment. Top row: Image after thin-plate spline transformation. Bottom row: Image after elastic transformation. An improvement in registration, compared to the thin-plate spline transformation, has been reached along the cortical boundary, and almost no improvement for the ventricles, since no appropriate input data were available.

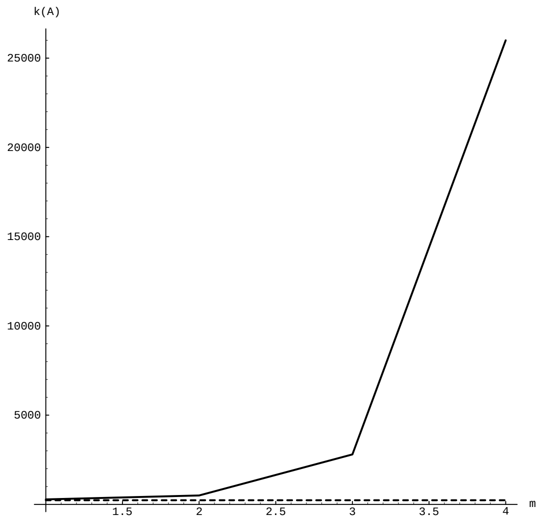

Figure 12: Dependence of the condition number on the parameter values. Solid line: Model of Davatzikos et al. [20]. Dashed line: Our approach. Since it contains no elastic parameters, the condition number of our approach remains constant.